PAPER

Check for updates

Impact of the crystalline phase of binary silicide on its lithiation and delithiation properties†

Yasuhiro Domi, [ID] [ab] Hiroyuki Usui, [ID] [ab] Takumi Ando[bc] and Hiroki Sakaguchi [ID] ⋆[ab]

In this work, we investigate the impact of the crystalline phase of binary silicide on its lithiation and delithiation properties. Charge–discharge testing shows that the reversible capacity is not dependent on the amount of Si included in the silicide; the capacity was found to be independent of the composition of the silicide even in the case of a given transition metal making up the silicide. The results of this study confirm that there is no phase separation of the silicide during the charge–discharge reactions. A high reversible capacity could be obtained when the affinity of the transition metal for Li was large and the distance between the Li atoms and the nearest-neighbour atom in lithiated silicide was large.

Introduction

Rechargeable batteries are essential to the transition toward building a carbon-neutral society. In particular, lithium-ion batteries (LIBs) are widely utilized as power sources across a wide range of applications.[1,2] LIBs are a mature and established technology, and their demand will not decrease rapidly even if new rechargeable batteries are developed in the future. However, although the material composition of current LIBs is excellent, there is still considerable potential for material development to improve the energy density of LIBs.

Silicon (Si) is an important active material for the negative electrodes of future LIBs because it has a high theoretical capacity of 3580 mA h g^{-1}; this value is considerably higher than that of graphite (372 mA h g^{-1}), which is currently used for this purpose. However, Si electrodes exhibit an inferior cycle life, which is primarily caused by a considerable change in volume during charge (lithiation) and discharge (delithiation).[3–5] To improve this poor cycle life, various approaches have been investigated. These include preparation of nano Si materials that alleviate the stress due to volumetric change;[4,6–8] covering Si with carbon materials to decrease the electrical resistivity;[6,9–11] doping of Si with impurities (such as phosphorous and arsenic) to change its properties, including phase transition, morphology, crystallinity, electronic conductivity and Li$^+$ diffusion;[5,12–16] synthesizing composites composed of binary or ternary silicide and pure Si to counter some of the drawbacks of Si;[17–27] and pre-lithiation of Si with the aim of increasing the initial Coulombic efficiency of the electrode.[28–32]

With the objective of overcoming the drawbacks of Si for applications as the negative electrode in LIBs, we synthesize pure binary silicides and investigate their charge and discharge properties as well as their reaction.[33,34] We find that some silicide electrodes exhibit a high discharge capacity and superior cyclability in an ionic liquid electrolyte. The discharge capacity correlates with the charge density of transition metals; when the affinity of the transition metal with Li is high, the capacity is high. Additionally, a surface film derived from an ionic liquid electrolyte is homogeneous and thin, which leads to uniform lithiation of Si. The superior cyclability results from the surface film properties. However, the impact of the different crystalline phases of the binary silicide on its lithiation and delithiation properties remains unclear. Herein, we aim to clarify the relationship between the crystalline phase of silicide (MSi_x, M: metal) and its charge–discharge properties. We focus on the use of Ni and Fe as M because NiSi$_2$ and FeSi$_2$ have a relatively high reversible capacity due to the high affinity of M with Li,[33] and these silicides have several different crystalline phases. We find promising Si-based active materials for negative electrodes in LIBs with high gravimetric and/or volumetric energy densities in this work.

^{a} Department of Chemistry and Biochemistry, Graduate School of Engineering, Tottori University, 4-101 Minami, Koyama-cho, Tottori 680-8552, Japan. E-mail: sakaguch@tottori-u.ac.jp

^{b} Centre for Research on Green Sustainable Chemistry, Tottori University, 4-101 Minami, Koyama-cho, Tottori 680-8552, Japan

^{c} Department of Engineering, Graduate School of Sustainability Science, Tottori University, 4-101 Minami, Koyama-cho, Tottori 680-8552, Japan

† Electronic supplementary information (ESI) available. See DOI: https://doi.org/10.1039/d2ma00171c

Experimental

Synthesis of silicides

We synthesized MSi_x (M = Ni or Fe, x = 2, 1, 1/2 or 1/3) powders *via* a mechanical alloying (MA) method using optimized conditions, as shown in Table S1 (ESI†). For the MA process, we used a high-energy planetary ball mill (P-6, Fritsch). The

elemental Si (99.9%) and iron (99.9%) powders were purchased from FUJIFILM Wako Pure Chemical Corporation, Ltd. Additionally, we obtained nickel (99.9%) from Nilaco Corporation. We placed a mixture of Si and M in a ZrO_2 container along with the ZrO_2 balls; the weight ratio of the balls and the mixture was approximately 15 : 1. The container was then filled with dry Ar gas. For treatment times of longer than 10 h, we opened the container in an Ar-filled glovebox and stirred the mixture using a spatula every 10 h.

Characterization

We confirmed the crystal structure of the synthesized powders using X-ray diffraction (XRD, Ultima IV, Rigaku), and we identified the obtained XRD patterns *via* comparison with those available on the Inorganic Crystal Structure Database (ICSD). Additionally, we confirmed the absence of elemental Si in the synthesized powders using Raman spectroscopy (NanofinderFLEX; Tokyo Instruments, Inc.); the absence of elemental Si is important as the properties of each silicide cannot be accurately evaluated if pure Si is present. We obtained the Raman spectra with the 532 nm line (16.5 mW) of a Nd:YAG laser through a $50\times$ objective lens. The average particle size of the synthesized powder was estimated using a particle size distribution analyser (SALD-2300, Shimadzu). The powder (*ca.* 0.1 g) was dispersed ultrasonically in 0.5 wt% sodium hexametaphosphate aqueous solution (approximately 10 ml). We analysed the particle size distribution by diluting the prepared suspension.

Electrode preparation by using a gas deposition method

We used the gas deposition (GD) method to prepare the silicide electrodes. Using this method, it is possible to investigate the original charge–discharge properties of active materials because the GD method requires no conductive agent or binder.[35,36] We used 99.9999% helium gas as a carrier gas. The conditions used in the GD process are reported in ref. 12 and 37. The weight of the deposited $M Si_x$ powder on a Cu current collector (thickness: 20 mm, Hohsen Corp.) was approximately 30 µg.

Coin cell assembly and charge–discharge testing

We assembled a 2032-type coin cell, which was composed of the electrode prepared *via* the GD method as the working electrode, a Li metal foil (thickness: 1 mm, 99.9%, Rare Metallic Co., Ltd) as the counter electrode, 1 mol dm^{-3} (M) lithium bis (fluorosulfonyl)amide (LiFSA) in N-methyl-N-propylpyrrolidinium bis (fluorosulfonyl)amide (Py13-FSA) as the electrolyte and a glass fibre filter (Whatman GF/A) as the separator in an Ar-filled glovebox (Miwa MFG, DBO-2.5LNKP-TS) with an oxygen content of less than 1 ppm and a dew point below $-90\,°C$. We chose 1 M LiFSA/Py13-FSA as the electrolyte because Si-based electrodes exhibited a superior cycling performance in 1 M LiFSA/Py13-FSA.[15,24,27,33] LiFSA and Py13-FSA were purchased from Kishida Chemical Co., Ltd and Kanto Chemical Co., Inc., respectively.

A galvanostatic lithiation–delithiation testing of the $M Si_x$ electrode was conducted using a battery charge/discharge system (HJ-1001SD8 and HJ-1001SM8A, Hokuto Denco Co., Ltd) at a temperature of 30 °C. The testing was performed in the potential range from 0.005 to 2.000 V *versus* Li$^+$/Li at a current

density of 50 mA g^{-1}. In the first cycle, the testing was carried out from an open circuit potential (OCP).

First principles calculation

A first principles calculation based on density functional theory (DFT) was carried out to investigate the charge density distribution in $Li_{0.25}M Si_x$ (M = Ni or Fe, x = 2, 1, 1/2 or 1/3), with the exception of $Li_{0.25}NiSi_{1/3}$, using the Advance/PHASE software package (Advance Soft Corp.). $Li_{1/3}NiSi_{1/3}$ was added to ensure that the number of Li atoms in each lattice was the same. The projector augmented wave (PAW) method was adopted, and the generalized gradient approximation (GGA) was employed as the term exchange correlation. Values of 112.5 and 12.5 Hartree were applied as the cutoff values for the charge densities and the wave functions, respectively.

Results and discussion

Synthesis of $NiSi_x$ and $FeSi_x$ with different crystalline phases

Fig. 1 shows XRD patterns of the powders synthesized from elemental Ni and Si with different mixture ratios. All of the diffraction peaks were consistent with the ICSD patterns of $NiSi_2$, $NiSi$, Ni_2Si or Ni_3Si, and no peaks that would indicate the presence of the raw materials (Si, Ni and Fe) were found. Similar results were obtained in the case of $FeSi_x$ (Fig. 2). The crystallite size of synthesized powders is summarized in Table S2 (ESI†).

Fig. 3 shows the Raman spectra of the prepared samples. Raman bands assigned to crystalline Si (*c*-Si) and amorphous Si (*a*-Si) appear in the obtained patterns.[38,39] $NiSi_x$ and $FeSi_x$ exhibited no Raman bands, and it can therefore be concluded that the synthesized powders contained neither *c*-Si nor *a*-Si.
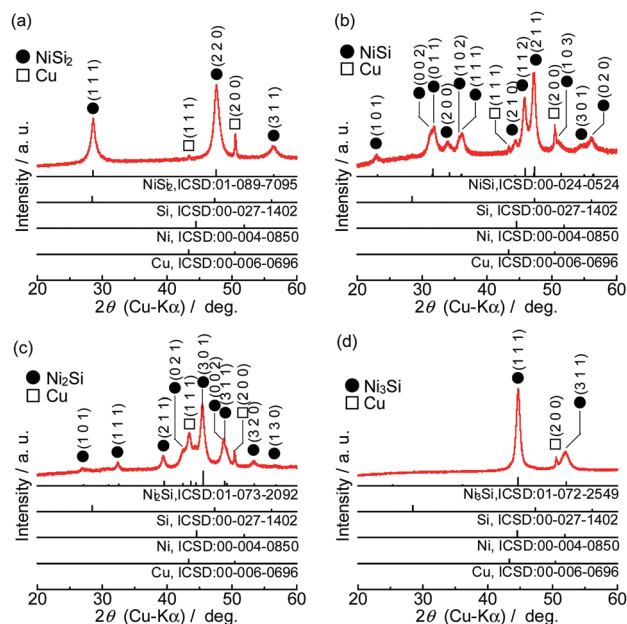

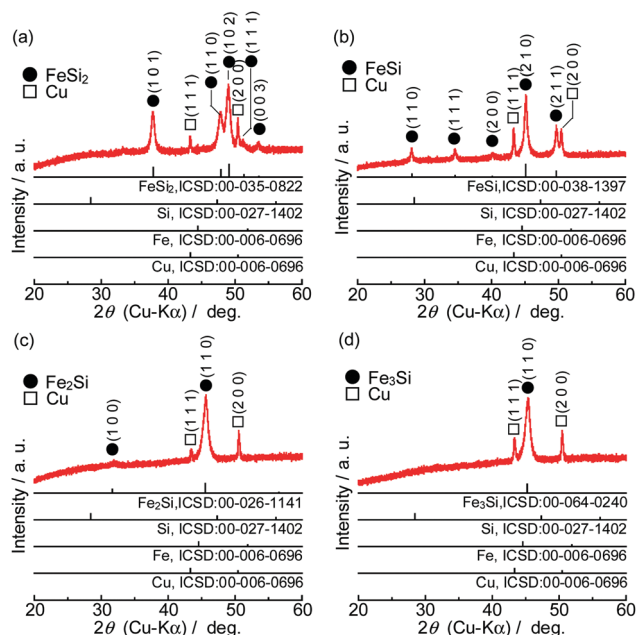**Fig. 1** XRD patterns of synthesized samples for (a) $NiSi_2$, (b) NiSi, (c) Ni_2Si and (d) Ni_3Si.

Fig. 2 XRD patterns of synthesized samples for (a) FeSi$_2$, (b) FeSi, (c) Fe$_2$Si and (d) Fe$_3$Si.
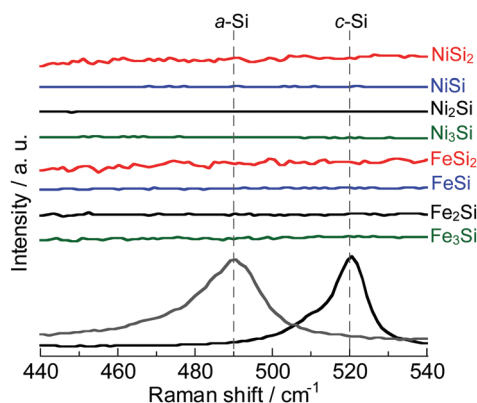

Fig. 3 Raman spectra of NiSi$_x$ and FeSi$_x$ (x = 2, 1, 1/2 and 1/3) powders. For comparison, the spectra of c-Si and a-Si are also shown.

These results demonstrate that the crystalline NiSi$_x$ and FeSi$_x$ phases were successfully formed *via* MA. The physical properties of each phase are summarized in Table S3 (ESI†),[40] and Fig. S1 and S2 (ESI†) show the crystal structure of NiSi$_x$ and FeSi$_x$ (x = 2, 1, 1/2 or 1/3) phases, respectively. Fig. 4 shows particle size distribution of NiSi$_2$ and FeSi$_2$. We can confirm that the average particle sizes of synthesized samples are almost the same. Hence, we can discuss the charge and discharge properties only by the difference in the crystalline phase.

Lithiation and delithiation properties of the NiSi$_x$ and FeSi$_x$ electrodes

Fig. 5 and 6 show the initial charge–discharge curves of the NiSi$_x$ and FeSi$_x$ (x = 2, 1, 1/2 or 1/3) electrodes in 1 M LiFSA/Py13-FSA, respectively. Herein, the specific capacity (mA h g^{-1})
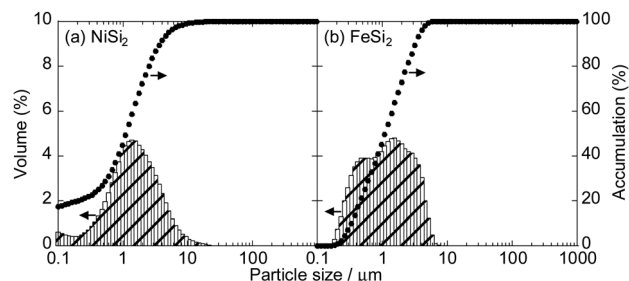

Fig. 4 Particle size distribution of (a) NiSi$_2$ and (b) FeSi$_2$ particles in 0.5 wt% sodium hexametaphosphate aqueous solution.

in the horizontal axis indicates the weight of active materials (silicides). All the electrodes exhibited a plateau in the potential between 1.5 and 1.0 V on the initial charge curve, which result from the reductive decomposition of the electrolyte that forms a surface film. Reductive decomposition of FSA anion on Si electrodes occurs at approximately 1.4 V *vs.* Li$^+$/Li.[41] The initial Coulombic efficiency was found to be low due to decomposition of large quantities of the electrolyte. The efficiency improved during the second and third cycles due to the suppression of electrolyte decomposition.

The initial Coulombic efficiencies of NiSi$_2$ and FeSi$_2$ were the highest between the NiSi$_x$ and FeSi$_x$ electrodes, respectively. It is considered that surface films with low electron conductivity formed on NiSi$_2$ and FeSi$_2$ electrodes. Silicate has been detected as a surface film component on Si-based electrodes even though the electrolyte has no Si component.[42] That is, a part of the active material can be a surface film, and hence, the composition of silicides should affect the reductive decomposition products of the electrolyte.

We could confirm potential slopes of less than 1.0 V on charge and discharge curves irrespective of the cycle number. It is well known that the alloying and dealloying reactions of Si electrodes with Li occur at approximately 0.1 and 0.4 V on charge and discharge curves, respectively.[43] Consequently, it
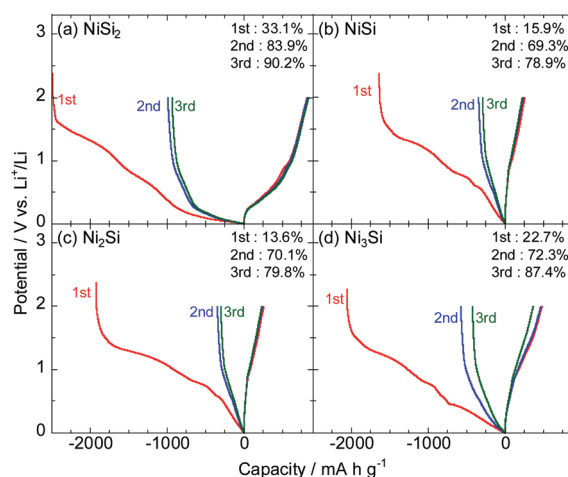

Fig. 5 Initial charge–discharge curves of (a) NiSi$_2$, (b) NiSi, (c) Ni$_2$Si and (d) Ni$_3$Si electrodes in 1 M LiFSA/Py13-FSA. The Coulombic efficiency in each cycle is shown in the upper right of subfigure.
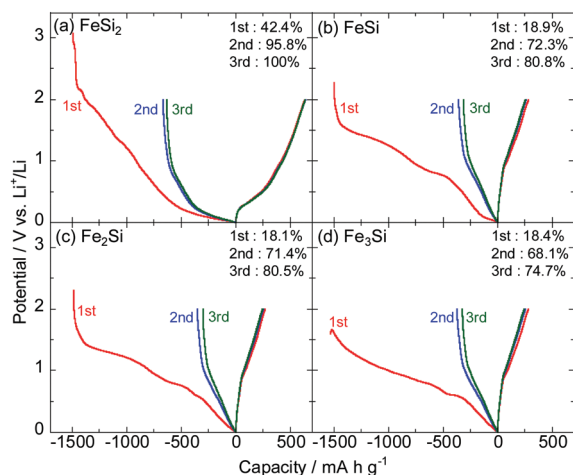
Fig. 6 Initial charge–discharge curves of for (a) $FeSi_2$, (b) FeSi, (c) Fe_2Si and (d) Fe_3Si electrodes in 1 M LiFSA/Py13-FSA. The Coulombic efficiency at each cycle is shown in the upper right of subfigure.

can be concluded that no phase separation of silicide (*e.g.*, $FeSi_2 + yLi^+ + ye^- \rightarrow Li_ySi_2 + Fe$ and/or $FeSi_2 + yLi^+ + ye^- \rightarrow Li_ySi + FeSi$) occurs and the silicide itself reacts with Li.[34]

Fig. 7a shows the dependence of the gravimetric discharge capacity of $NiSi_x$ (x = 2, 1, 1/2 or 1/3) electrodes on the cycle number in 1 M LiFSA/Py13-FSA. The corresponding capacity retention is also shown in Fig. S3 (ESI†). The initial capacity was found to be independent on the value of x; the $NiSi_2$ electrode was found to exhibit the highest reversible capacity of over 800 mA h g^{-1}, and the Ni_3Si electrode was found to have the middle capacity of approximately 400 mA h g^{-1}. Additionally, the NiSi and Ni_2Si electrodes were found to have a lower initial capacity of 200 mA h g^{-1}. The fact that $NiSi_2$ has the highest initial discharge capacity among the four $NiSi_x$ indicates that $NiSi_2$ alloys and dealloys with more Li. Hence, the change in $NiSi_2$ volume is larger compared to those of the other nickel silicides and the electrode disintegration should occur, which results in capacity fading.

High volumetric capacity is also essential for the fabrication of small batteries. The densities of $NiSi_2$, NiSi, Ni_2Si and Ni_3Si are 4.83, 5.96, 7.37 and 7.84 g cm^{-3}, respectively; the density of $NiSi_x$ increases with decreasing values of x. Fig. 7b shows the dependence of the volumetric discharge capacity of the $NiSi_x$ electrodes on the cycle number. It is generally the case that the gravimetric capacity is represented per mass of the unlithiated active material, whereas the volumetric capacity is frequently expressed per volume of the fully lithiated material.[44] However, the precise Li amount alloyed with $NiSi_x$ is unclear;[33] thus, the capacity per volume of Li-free silicide is reported here. That is, the volumetric capacity is expressed as the product of the gravimetric capacity and the density. At the 300th cycle, the volumetric capacity of the Ni_3Si electrode exceeded that of the $NiSi_2$ electrode; the Ni_3Si electrode thus exhibited a superior cycle stability and should be a promising negative electrode for LIBs with high volumetric energy density.
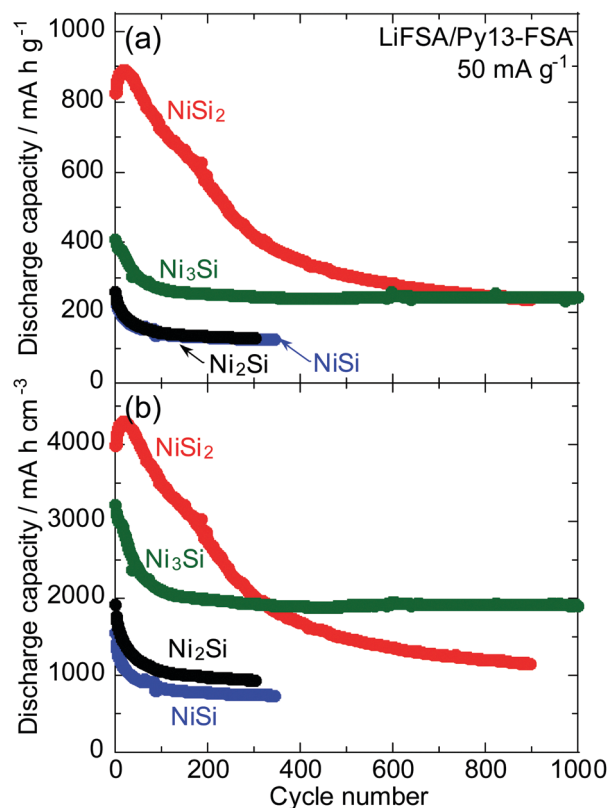

Fig. 7 Dependence of (a) the gravimetric and (b) the volumetric discharge capacity of $NiSi_x$ (x = 2, 1, 1/2 and 1/3) electrodes on the cycle number under a current density of 50 mA g^{-1} in 1 M LiFSA/Py13-FSA.

Fig. 8 shows cycling performance of the $FeSi_x$ electrodes in 1 M LiFSA/Py13-FSA. The corresponding capacity retention was also shown in Fig. S4 (ESI†). The $FeSi_2$ electrode exhibited the highest gravimetric and volumetric reversible capacities among the four $FeSi_x$ electrodes. The gravimetric discharge capacities of the other electrodes (FeSi, Fe_2Si and Fe_3Si) were found to be similar. The Fe_3Si electrode also showed slightly higher volumetric capacity compared to the FeSi electrode because the former has larger density. It should be noted that volumetric discharge capacity of the Fe_2Si electrode cannot be calculated because the density of Fe_2Si is unclear.

It has been previously reported that the silicide phase does not separate into Si and metal and/or Si-poor silicide phases during charge–discharge processes; the reversible capacity is not obtained by lithiation and delithiation of the Si phase.[34] Fig. 7 and 8 demonstrated that the discharge capacity is not correlated with the amount of Si included in the silicide. This result also reaffirms that no phase separation of silicide occurs during charge–discharge reactions.

Charge density distribution and distance between Li and nearest-neighbour atom

Here, we investigated the cause of the differing discharge capacity in the crystalline phase based on computational chemistry, despite the silicide being composed of the same metal and Si. Herein, we calculated charge density of each
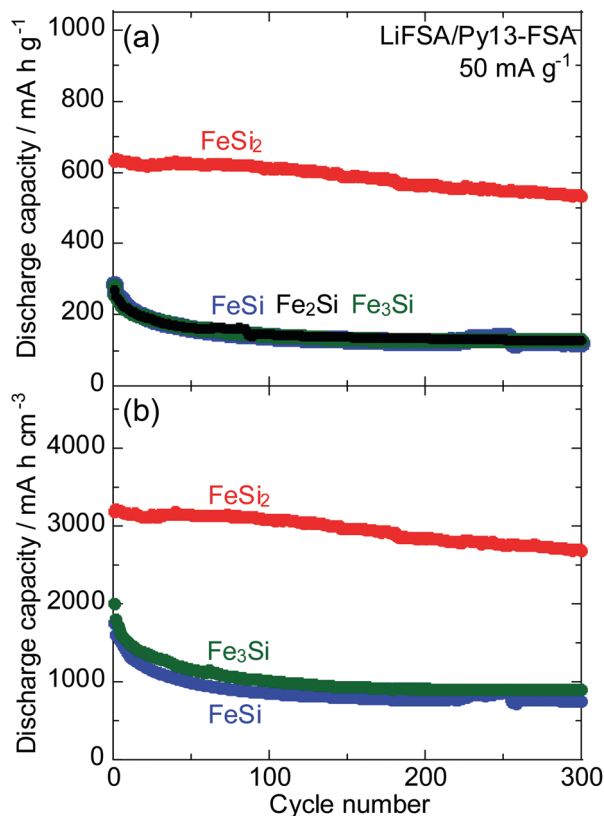
Fig. 8 Dependence of (a) the gravimetric and (b) the volumetric discharge capacity of $FeSi_x$ (x = 2, 1, 1/2 and 1/3) electrodes on the cycle number under a current density of 50 mA g^{-1} in 1 M LiFSA/Py13-FSA.

element in lithiated $NiSi_x$ (x = 2, 1, 1/2 or 1/3, Table 1). Fig. S5 (ESI†) also shows the crystal structure of each lithiated $NiSi_x$. We could not perform the corresponding calculation for lithiated $FeSi_x$ since the crystal structure of lithiated $FeSi_x$ was optimized only for lithiated $FeSi_2$. It has previously reported that the reversible capacity increases when the affinity of the metal composed making up the silicide for Li is large.[33] Here, the affinity is defined as the difference in charge density between Li and the metal.

In Table 1, $Li_{0.25}NiSi_2$ is seen to have the largest affinity of Ni for Li and the highest initial discharge capacity. By contrast, $Li_{0.25}NiSi$, $Li_{0.25}Ni_2Si$ and $LiNi_3Si$ are seen to have very similar affinities, whereas the $Li_{0.25}NiSi$ and $Li_{0.25}Ni_2Si$ are seen to have the lowest initial capacity and the $LiNi_3Si$ exhibits the middle capacity; this difference in capacity cannot be explained only by the affinity between Ni and Li. Hence, we investigate the

Table 1 Charge density of each element in lithiated $NiSi_x$ (x = 2, 1, 1/2 or 1/3)

	Li	Si	Ni	Initial discharge capacity/ mAh g^{-1}
$Li_{0.25}NiSi_2$	+0.78	+0.40	−1.00	824
$Li_{0.25}NiSi$	+0.52	+0.35	−0.48	260
$Li_{0.25}Ni_2Si$	+0.61	+0.55	−0.35	261
$LiNi_3Si$	+0.63	+0.52	−0.39	410

Table 2 Distance between Li and nearest-neighbour atom in lithiated $NiSi_x$ (x = 2, 1, 1/2 or 1/3)

	Distance/nm	Initial discharge capacity/ mAh g^{-1}
$Li_{0.25}NiSi_2$	0.234	824
$Li_{0.25}NiSi$	0.134	260
$Li_{0.25}Ni_2Si$	0.172	261
$LiNi_3Si$	0.175	410

distance between the Li atoms and its nearest–neighbour atoms in the lithiated $NiSi_x$ (Table 2 and Fig. S6, ESI†). The $Li_{0.25}NiSi_2$ was found to have the largest distance, $Li_{0.25}Ni_2Si$ and $LiNi_3Si$ showed middle distances, and the distance of $Li_{0.25}NiSi$ was the shortest. When the distance is large, the capacity tends to be larger; under this condition, the Li atoms should be relatively free to move in the silicide and diffuse evenly. Focusing again on the affinity of $Li_{0.25}Ni_2Si$ and $LiNi_3Si$, the latter exhibited a higher value. Consequently, the difference in the capacity of silicide can be understood by considering both the affinity of metal that makes up the silicide for Li and the distance between Li and nearest-neighbour atom in lithiated silicide.

Conclusions

In the present study, we synthesized various pure binary silicides in which the crystalline phase differed using the same metal, and investigated the impact of the crystalline phase of silicide on its lithiation and delithiation properties. The $NiSi_2$ electrode exhibited the highest reversible capacity of over 800 mA h g^{-1} and the Ni_3Si electrode was found to have the middle capacity. NiSi and Ni_2Si electrodes were also found to have a lower initial capacity. The Ni_3Si electrode should be a promising negative electrode for LIBs with high volumetric energy density. By contrast, the $FeSi_2$ electrode exhibited the highest discharge capacity among the four $FeSi_x$ electrodes, and the capacities of other FeSi, Fe_2Si and Fe_3Si electrodes were found to be very similar. Therefore, it was concluded that the reversible capacity was unrelated to the amount of Si included in the silicide; the capacity differed depending on x in MSi_x even if M was the same. The results confirmed that no phase separation of the silicide occurred during the charge–discharge reactions. A high discharge capacity was generally found when the affinity of M which made up the silicide for Li was large and the distance between Li and the nearest-neighbour atom in lithiated MSi_x was large.

Author contributions

The manuscript was written through the contributions of all authors.

Conflicts of interest

There are no conflicts to declare.

Acknowledgements

Notes and references

1 M. S. Whittingham, *Chem. Rev.*, 2004, **104**, 4271–4301.
2 M. Armand and J.-M. Tarascon, *Nature*, 2008, **451**, 652–657.
3 M. N. Orrovac and L. J. Krause, *J. Electrochem. Soc.*, 2007, **154**, A103–A108.
4 X. H. Liu, L. Zhong, S. Huang, S. X. Mao, T. Zhu and J. Y. Huang, *ACS Nano*, 2012, **6**, 1522–1531.
5 Y. Domi, H. Usui, K. Yamaguchi, S. Yodoya and H. Sakaguchi, *ACS Appl. Mater. Interfaces*, 2019, **11**, 2950–2960.
6 U. Kasavajjula, C. Wang and A. J. Appleby, *J. Power Sources*, 2007, **163**, 1003–1039.
7 B. Hertzberg, A. Alexeev and G. Yushin, *J. Am. Chem. Soc.*, 2010, **132**, 8548–8549.
8 B. Liang, Y. Liu and Y. Xu, *J. Power Sources*, 2014, **267**, 469–490.
9 L.-F. Cui, R. Ruffo, C. K. Chan, H. Peng and Y. Cui, *Nano Lett.*, 2009, **9**, 491–495.
10 L.-F. Cui, Y. Yang, C.-M. Hsu and Y. Cui, *Nano Lett.*, 2009, **9**, 3370–3374.
11 N. Liu, H. Wu, M. T. McDowell, Y. Yao, C. Wang and Y. Cui, *Nano Lett.*, 2012, **12**, 3315–3321.
12 Y. Domi, H. Usui, M. Shimizu, Y. Kakimoto and H. Sakaguchi, *ACS Appl. Mater. Interfaces*, 2016, **8**, 7125–7132.
13 S. Huang, L.-Z. Cheong, D. Wang and C. Shen, *ACS Appl. Mater. Interfaces*, 2017, **9**, 23672–23678.
14 W.-C. Chang, K.-W. Tseng and H.-Y. Yuan, *Nano Lett.*, 2017, **17**, 1240–1247.
15 S. Yodoya, Y. Domi, H. Usui and H. Sakaguchi, *ChemistrySelect*, 2019, **4**, 1375–1378.
16 D. Lau, C. A. Hall, S. Lim, J. A. Yuwano, P. A. Burr, N. Song and A. Lennon, *ACS Appl. Energy Mater.*, 2020, **3**, 1730–1741.
17 H. Sakaguchi, T. Iida, M. Itoh, N. Shibamura and T. Hirono, *IOP Conf. Ser.: Mater. Sci. Eng.*, 2009, **1**, 012030.
18 H. Usui, K. Maebara, K. Nakai and H. Sakaguchi, *Int. J. Electrochem. Sci.*, 2011, **6**, 2246–2254.
19 H. Usui, M. Nomura, H. Nishino, M. Kusatsu, T. Murota and H. Sakaguchi, *Mater. Lett.*, 2014, **130**, 61–64.
20 H. Usui, K. Nouno, Y. Takemoto, K. Nakada, A. Ishii and H. Sakaguchi, *J. Power Sources*, 2014, **268**, 848–852.
21 Y. Domi, H. Usui, Y. Takemoto, K. Yamaguchi and H. Sakaguchi, *J. Phys. Chem. C*, 2016, **120**, 16333–16339.
22 Y. Domi, H. Usui, Y. Takemoto, K. Yamaguchi and H. Sakaguchi, *Chem. Lett.*, 2016, **45**, 1198–1200.
23 Y. Domi, H. Usui, E. Nakabayashi, Y. Kimura and H. Sakaguchi, *ACS Appl. Energy Mater.*, 2020, **3**, 7438–7444.
24 Y. Domi, H. Usui, Y. Shindo, S. Yodoya, H. Sato, K. Nishikawa and H. Sakaguchi, *Electrochemistry*, 2020, **88**, 548–554.
25 Y. Kimura, Y. Domi, H. Usui and H. Sakaguchi, *Electrochemistry*, 2020, **88**, 330–332.
26 Y. Kimura, Y. Domi, H. Usui and H. Sakaguchi, *ACS Omega*, 2021, **6**, 8862–8869.
27 Y. Domi, H. Usui, K. Nishikawa and H. Sakaguchi, *ACS Appl. Nano Mater.*, 2021, **4**, 8473–8481.
28 N. Liu, L. Hu, M. T. McDowell, A. Jackson and Y. Cui, *ACS Nano Lett.*, 2011, **5**, 6487–6493.
29 T. Okubo, M. Saito, C. Yodoya, A. Kamei, M. Horita, T. Takenaka, T. Okumura, A. Tasaka and M. Inaba, *Solid State Ionics*, 2014, **262**, 39–42.
30 Y. Domi, H. Usui, D. Iwanari and H. Sakaguchi, *J. Electrochem. Soc.*, 2017, **164**, A1651–A1654.
31 M. Saito, K. Kato, S. Ishii, K. Yoshii, M. Shikano, H. Sakaebe, H. Kiuchi, T. Fukunaga and E. Matsubara, *J. Electrochem. Soc.*, 2019, **166**, A5174–A5183.
32 Y. Domi, H. Usui, N. Ieuji, K. Nishikawa and H. Sakaguchi, *ACS Appl. Mater. Interfaces*, 2021, **13**, 3816–3824.
33 Y. Domi, H. Usui, R. Takaishi and H. Sakaguchi, *ChemElectroChem*, 2019, **6**, 581–589.
34 Y. Domi, H. Usui, K. Sugimoto, K. Gotoh, K. Nishikawa and H. Sakaguchi, *ACS Omega*, 2020, **5**, 22631–22636.
35 H. Sakaguchi, T. Toda, Y. Nagao and T. Esaka, *Electrochem. Solid-State Lett.*, 2007, **10**, J146–J149.
36 H. Usui, Y. Kiri and H. Sakaguchi, *Thin Solid Films*, 2012, **520**, 7006–7010.
37 Y. Domi, H. Usui, M. Shimizu, K. Miwa and H. Sakaguchi, *Int. J. Electrochem. Sci.*, 2015, **10**, 9678–9686.
38 M. Shimizu, H. Usui, T. Suzumura and H. Sakaguchi, *J. Phys. Chem. C*, 2015, **119**, 2975–2982.
39 K. Yamaguchi, Y. Domi, H. Usui and H. Sakaguchi, *ChemElectroChem*, 2017, **4**, 3257–3263.
40 C. Tang, F. Wen, H. Chen, J. Liu, G. Tao, N. Xu and J. Xue, *J. Alloys Compd.*, 2019, **778**, 972–981.
41 K. Yamaguchi, Y. Domi, H. Usui, M. Shimizu, K. Matsumoto, T. Nokami, T. Itoh and H. Sakaguchi, *J. Power Sources*, 2017, **338**, 103–107.
42 Y. Kimura, Y. Domi, H. Usui and H. Sakaguchi, *J. Electrochem. Soc.*, 2022, **169**, 010537.
43 V. L. Chevrier, J. W. Zwanziger and J. R. Dahn, *J. Alloys Compd.*, 2010, **496**, 25–36.
44 N. Nitta and G. Yushin, *Part. Part. Syst. Charact.*, 2014, **31**, 317–336.